

EFFECTS OF MICROSTRUCTURE ON RESISTANCE TO SHEAR LOCALIZATION FOR A CLASS OF METAL MATRIX COMPOSITES

M. ZHOU

The George W. Woodruff School of Mechanical Engineering, Georgia Institute of Technology, Atlanta, GA 30332-0405, USA

Abstract—The development of shear bands in a class of materials with inhomogeneous and composite microstructures is analysed using dynamic finite element calculations. The analysis is based on experimental studies of the deformation localization and constitutive behaviour of tungsten composites having two-phase microstructures consisting of hard tungsten grains and a soft alloy metal matrix. The calculations concern the effects of variations in microstructures on the resistance of the materials to shear banding. Specifically, three variations from the currently used microstructure are considered: (1) the alteration of the matrix phase to one that has a lower thermal conductivity; (2) the introduction of an interfacial layer between the grains and the matrix which limits microscopic heat exchange between the phases by having a low thermal conductivity; and (3) the modification of the matrix to one having a lower strength at high temperatures, but otherwise the same thermal and mechanical properties as the nickel–iron–tungsten matrix currently used in many tungsten composites. Numerical results show that the introduction of the low-conductivity interfacial layer significantly enhances the formation of shear bands and reduces the overall flow stress of the composite throughout the deformation. On the other hand, accelerated thermal softening of the matrix phase at high temperatures expedites localization in later stages of deformation while allowing the material to maintain a strong stress–strain response in the early part of the deformation. The results point out possible directions for the improvement of advanced composites in applications where the localization of deformation plays an important role.

Keywords—Shear localization; Microstructural effect; Metal matrix composites; Numerical modelling.

INTRODUCTION

The localization of dynamic deformation into bands of high rates of shear strain and high temperatures is a phenomenon that plays an important role in many applications. These shear bands represent a mechanism for deformation, failure and energy dissipation. Depending on the specific application, the formation of these bands is either a mode of failure that should be avoided or a means to achieve a certain type of performance, therefore should be promoted to occur. One application in which shear bands are desired is kinetic energy penetrators of heavy armour. It has been found that the performance of penetrators depends strongly on the formation of shear bands [1]. Specifically, the localization of plastic deformation associated with the development of shear bands and the eventual material failure inside the bands significantly improve the performance of the penetrators by allowing deformed materials to be discarded from the enlarged penetrator head, thereby preserving the sharp front of the projectiles. A sharp front corresponds to larger depths of penetration. Conversely, excessive mushrooming of the projectiles, and the resulting reduction in penetrator performance have been associated with relatively weak propensities of penetrator materials for forming shear bands. The materials involved are tungsten-based composites, e.g. the W–Ni–Fe composite used in the study of Zhou *et al.* [2–4]. Although shear bands have been observed to form in the W–Ni–Fe composites, see e.g. [2–6], they show relatively weak performance as a penetrator material compared with depleted uranium (DU), which has been the traditional material for penetrators. In order for these composites to replace DU (which causes environmental and handling concerns due to its slight radioactivity) as a penetrator material, their ability to form shear bands has to be improved. The composite nature of the microstructures offers opportunities

for microstructural revision and engineering. One way to facilitate the development of shear bands in these materials is to alter their microstructures. Currently, most of the microstructures consist of hard tungsten grains embedded in a softer and more ductile matrix phase which is, e.g. an alloy like Ni–Fe–W, Ni–Co or Ni–Mn.

A pressure–shear plate impact experiment was used in Refs [2–4] to analyse the formation of shear bands in a tungsten composite having a composition of 93% tungsten, 4.9% Ni and 2.1% Fe by weight. This configuration (Fig. 1) subjects the material to dynamic shear loading at shear strain rates of the order of 10^5 – 10^6 s⁻¹. The high rates of loading in excess of 10^5 s⁻¹ are achieved by sandwiching a thin foil specimen between two hard elastic plates. The parallel impact faces are inclined relative to the direction of approach to achieve combined pressure–shear loading. Before unloading waves arrive from lateral boundaries, the stress and deformation states are characterized by plane wave conditions, and the histories of nominal normal and shear stresses, strains and strain rates can be experimentally determined, therefore allowing the evolution of deformation and the load-carrying capacity of the specimen material to be obtained.

The experimental and numerical analyses demonstrated the effects of several different microstructures on the overall behaviour of the tungsten composite. It was found that material inhomogeneities inherent in the composite microstructure enhance the propensity to form shear bands. The study further demonstrated that the conduction of heat significantly stabilizes deformation in the composite microstructures of this class of materials. Without heat conduction, shear bands develop significantly more rapidly than when heat conduction was considered. This finding pointed out possible means to engineer advanced composite materials with higher resistance to shear banding through the enhancement of microscopic heat exchange. Conversely, for applications in which shear banding is desired, inhibition of heat flow between microscopic phases may improve the performance of composites.

The objective of this paper is to examine several specific variations in the microstructures and characterize their effects on the development of shear bands. The effect of these changes on the evolution of the load-carrying capacity of the materials will also be analysed. The study uses finite element calculations that consider the microstructural profiles of the materials. Characterizations of the constitutive behaviour of the individual material constituents in the composites is based on experiments conducted under conditions similar to those found in actual penetration. Such conditions involve pressures up to 8–10 GPa and strain rates up to 10^6 s⁻¹. It is hoped that the analysis will suggest microstructural variations that may be used to engineer new and improved composite materials. The choice of the variations considered here is motivated by the need for enhanced propensity for shear localization in the penetrator application of tungsten composites. The choice is also partly based on the results of the previous study which demonstrated that heat exchange between microstructural constituents strongly influences the localization of deformation in the materials analysed here.

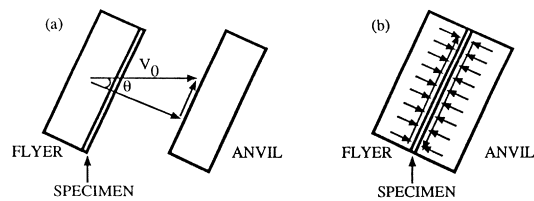


Fig. 1. Pressure–shear impact experiment of a thin specimen; (a) schematic of the pressure–shear plate impact configuration; (b) combined normal and transverse loading on the specimen material.

PROBLEM ANALYSED

Because shear banding contributes to improving the performance of penetrators, the current analysis focuses on changes in the microstructures of these composites that may enhance the localization of deformation. It is hoped that useful microstructural changes can be identified and their effects characterized. The specific changes analysed here involve the retardation of microscopic heat conduction and the use of higher rates of thermal softening. Four different microstructural configurations are considered in the analysis carried out. These four cases are listed in Table 1. They are based on the two microstructural profiles shown in Fig. 2. For comparison purposes, the microstructural properties of a currently used tungsten composite (the same as that in Ref. [3]) are used as the basis from which variations are made. The morphology of the phases in the base microstructure is the grain–matrix arrangement of this actual tungsten composite, as shown in Fig. 2(a). This is the base microstructure analysed and is denoted as microstructure (a) in Table 1.

The base microstructure represents a material typical of those currently produced by industry. Three variations from this base microstructure are considered in the analysis. The first variation is the alteration of the matrix in the base microstructure to one that has a lower thermal conductivity, from $k = 100 \text{ W(m} \cdot \text{K)}^{-1}$ to $k = 25 \text{ W(m} \cdot \text{K)}^{-1}$. The modified matrix otherwise has the same properties as that in the base microstructure. This microstructure is referred to as microstructure (b) in Table 1 and has the grain–matrix morphology of Fig. 2(a), the same as the base microstructure. The second variation is the introduction of an interfacial layer into the base microstructure. The interfacial layer is between the grains and the matrix, and has a thickness of approximately $1 \mu\text{m}$. In order to delineate the influence of changes in thermal properties on the

Table 1. Microstructural variations

Microstructure	k_m [$\text{W(m} \cdot \text{K)}^{-1}$]	T_c [K]	T_m [K]	Phase morphology
(a) Base microstructure	100	1300	1750	Fig. 2(a)
(b) Matrix with low conductivity	25	1300	1750	Fig. 2(a)
(c) Additional interfacial layer	10	1300	1750	Fig. 2(b)
(d) Matrix with enhanced thermal softening at high temperatures	100	1000	1400	Fig. 2(a)

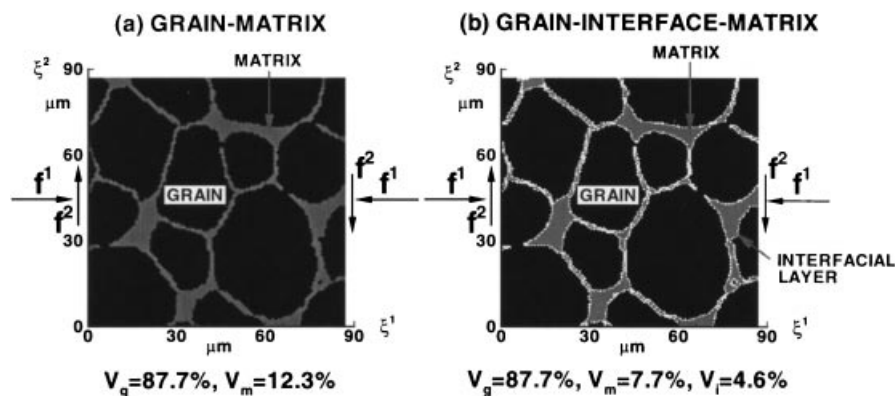


Fig. 2. Microstructural phase morphologies analysed; (a) grain–matrix morphology of an actual tungsten composite consisting of grains and matrix, (b) hypothetical grain–interface–matrix morphology obtained from (a) by adding an interfacial layer between the grains and matrix. The arrows indicate directions of boundary tractions applied during the numerical calculations and the experiments.

localization process, it is assumed that this layer has the same thermal and mechanical properties as the matrix phase, except its thermal conductivity. For the matrix, the thermal conductivity is $k = 100 \text{ W(m} \cdot \text{K)}^{-1}$ and for the interfacial layer $k = 10 \text{ W(m} \cdot \text{K)}^{-1}$. This layer retards heat exchange between the grains and the matrix due to its low thermal conductivity. This microstructure is referred to as microstructure (c) in Table 1. The grain–interface–matrix morphology of this microstructure is shown in Fig. 2(b). The third variation from the base microstructure is the modification of the matrix to one that has a higher rate of thermal softening at high temperatures than the matrix in the base microstructure. The difference in the thermal softening rates exists only for temperatures above 1000 K. This microstructure has otherwise the same thermal and mechanical properties as the Ni–Fe–W matrix in the base microstructure. The morphology of this grain–matrix composite is the same as the base microstructure [Fig. 2(a)]. This microstructure is referred to as microstructure (d) in Table 1.

The two microstructural phase morphologies in Fig. 2 have the same grain volume fraction of 87.7%. The matrix phase in Fig. 2(a) has a volume fraction of 12.3%. In Fig. 2(b), the matrix has a volume fraction of 7.7% and the interfacial layer has a volume fraction of 4.6%.

Characterization of the behaviour of the individual phases is based on data from pressure–shear plate impact, torsional Kolsky bar and quasi-static torsion experiments [2,4]. These experiments allowed the response over a wide range of strain rate, from 10^{-4} to $7 \times 10^5 \text{ s}^{-1}$, to be determined. At strain rates below 10^4 s^{-1} , the grains and the matrix have similar rate sensitivities of flow stress. The matrix exhibits lower strain rate sensitivity than the grains at strain rates above 10^4 s^{-1} . The matrix has a much higher rate of strain hardening than the grain material. The grains have a higher density, higher yield stress and lower specific heat compared with the matrix phase. To characterize the thermal softening behaviour, it is assumed that the stress-carrying capacity of each material vanishes when the temperature reaches the corresponding melting point. Partly because of their high melting temperatures, the tungsten grains have much lower rates of thermal softening than the matrix. The thermal softening behaviour of the three material constituents (grains, matrix and interfacial layer) are illustrated in Fig. 3. The enhanced thermal softening rate for the matrix in microstructure (d) is an assumed behaviour used in the analysis. Results will show that this higher rate of stress decrease with temperature at high temperatures does have a clear and significant influence on strain localization.

The response of the interfacial layer in microstructure (c) and the variations in the response of the matrix phase in microstructures (b) and (d) are assumed properties to allow the influence of such hypothetical microstructures on localization and evolution of stress-carrying capacities to be explored computationally. This analysis is intended to outline the effects of microstructural

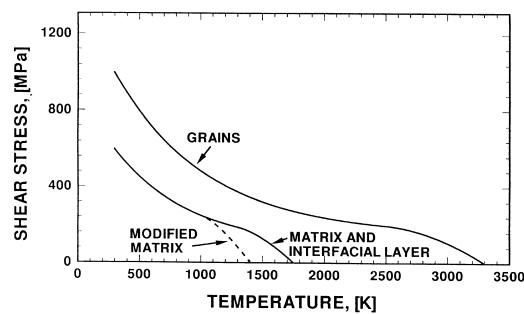


Fig. 3. An illustration of the temperature dependence of flow stress for the grains, matrix and interfacial layer.

variations on localization. The variations considered do not necessarily represent properties of specific material systems currently available.

The responses of the three material constituents in the four composite microstructures are characterized by the following thermo-viscoplastic relations

$$\left. \begin{aligned} \dot{\bar{\epsilon}} &= \frac{\dot{\epsilon}_1 \dot{\epsilon}_2}{\dot{\epsilon}_1 + \dot{\epsilon}_2}, & \dot{\epsilon}_1 &= \dot{\epsilon}_0 \left[\frac{\bar{\sigma}}{g(\bar{\epsilon}, T)} \right]^m, & \dot{\epsilon}_2 &= \dot{\epsilon}_m \exp \left[- \frac{ag(\bar{\epsilon}, T)}{\bar{\sigma}} \right], \\ g(\bar{\epsilon}, T) &= \sigma_0 \left(1 + \frac{\bar{\epsilon}}{\epsilon_0} \right)^N \left\{ 1 - \beta \left[1 - \exp \left(- \frac{T - T_0}{T_d} \right) \right] \right\} s(T), \\ s(T) &= \begin{cases} 1, & T \leq T_c, \\ \left[1 - \left(\frac{T - T_c}{T_m - T_c} \right)^2 \right], & T_c \leq T \leq T_m. \end{cases} \end{aligned} \right\} \quad (1)$$

In the above equations, $\bar{\epsilon} = \int_0^t \dot{\bar{\epsilon}} dt$ is the equivalent plastic strain, $\dot{\epsilon}_0$ is a reference strain rate, $\bar{\sigma}$ is the Mises equivalent stress, m and a are rate sensitivity parameters, respectively, for strain rates below 10^3 s^{-1} and above $5 \times 10^4 \text{ s}^{-1}$, σ_0 is a reference stress, ϵ_0 is a reference strain, N is a strain hardening exponent, T_0 is a reference temperature, and β and T_d are thermal softening parameters. Function $g(\bar{\epsilon}, T)$ represents the stress-strain relation at a quasi-static strain rate of $\dot{\epsilon}_0$ and at temperature T . At $T = T_0$, $g(\bar{\epsilon}, T_0) = \sigma_0(1 + \bar{\epsilon}/\epsilon_0)^N$. Function $s(T)$ is introduced to model higher rates of thermal softening at higher temperatures. T_c is a threshold temperature for $s(T)$ to become active, and T_m is the melting temperature. Model parameters for the constituent phases and the hypothetical interfacial layer for the four microstructures are listed in Tables 1 and 2.

ANALYTICAL FORMULATION

Momentum and energy balance

A convected coordinate, Lagrangian formulation of the field equations is used as, e.g. in Refs [7–9]. The independent variables are the particle coordinates, ξ^i , in the initial stress free

Table 2. Material parameters

Parameter	Grains	Matrix	Interface
$\dot{\epsilon}_0$	$1.0 \times 10^{-4} \text{ s}^{-1}$	$1.0 \times 10^{-4} \text{ s}^{-1}$	$1.0 \times 10^{-4} \text{ s}^{-1}$
m	50	17	17
σ_0	730 MPa	100 MPa	100 MPa
$\dot{\epsilon}_m$	$8.0 \times 10^8 \text{ s}^{-1}$	$8.0 \times 10^{10} \text{ s}^{-1}$	$8.0 \times 10^{10} \text{ s}^{-1}$
a	21	1	1
ϵ_0	1.83×10^{-5}	3.92×10^{-4}	3.92×10^{-4}
N	0.05	0.20	0.20
β	0.85	0.85	0.85
T_0	293 K	293 K	293 K
T_d	600 K	600 K	600 K
k	$160 \text{ W(m} \cdot \text{K)}^{-1}$	$100 \text{ W(m} \cdot \text{K)}^{-1}$ $25 \text{ W(m} \cdot \text{K)}^{-1}$	$10 \text{ W(m} \cdot \text{K)}^{-1}$ $10 \text{ W(m} \cdot \text{K)}^{-1}$
c_p	$138 \text{ J(kg} \cdot \text{K)}^{-1}$	$382 \text{ J(kg} \cdot \text{K)}^{-1}$	$382 \text{ J(kg} \cdot \text{K)}^{-1}$
χ	0.9	0.9	0.9
ρ	$19\,300 \text{ kg m}^{-3}$	9200 kg m^{-3}	9200 kg m^{-3}
E	$4.00 \times 10^5 \text{ MPa}$	$2.55 \times 10^5 \text{ MPa}$	$2.55 \times 10^5 \text{ MPa}$
ν	0.29	0.29	0.29
α	$5.3 \times 10^{-6} \text{ K}^{-1}$	$1.5 \times 10^{-5} \text{ K}^{-1}$	$1.5 \times 10^{-5} \text{ K}^{-1}$

configuration (see Fig. 2) and time, t . A material point initially at \mathbf{x} in the reference configuration assumes a position $\bar{\mathbf{x}}$ in the current configuration. The displacement vector \mathbf{u} and the deformation gradient tensor are defined by

$$\mathbf{u} = \bar{\mathbf{x}} - \mathbf{x}, \quad \mathbf{F} = \frac{\partial \bar{\mathbf{x}}}{\partial \mathbf{x}}. \quad (2)$$

The dynamic deformation of materials is a coupled thermomechanical process. The mechanical part is governed by the balance of momentum and the thermal part is governed by the balance of energy (heat equation). These two systems of equations are written as the principle of virtual work

$$\int_V \boldsymbol{\tau} : \delta \mathbf{D} \, dV = \int_S \mathbf{f} \cdot \delta \dot{\mathbf{u}} \, dS - \int_V \rho \frac{\partial^2 \mathbf{u}}{\partial t^2} \cdot \delta \dot{\mathbf{u}} \, dV, \quad (3)$$

and the variational heat equation

$$\begin{aligned} \int_V \rho c_p \dot{T} \delta T \, dV = & \int_V \chi \boldsymbol{\tau} : \mathbf{D}^p \delta T \, dV + \int_S k \left(\mathbf{F}^{-1} \cdot \mathbf{F}^{-T} \cdot \frac{\partial T}{\partial \mathbf{x}} \right) \cdot \mathbf{n} \delta T \, dS \\ & - \int_V k \left(\mathbf{F}^{-1} \cdot \mathbf{F}^{-T} \cdot \frac{\partial T}{\partial \mathbf{x}} \right) \cdot \frac{\partial \delta T}{\partial \mathbf{x}} \, dV, \end{aligned} \quad (4)$$

where V , S and ρ are the volume, surface and mass density, respectively, of the body in the reference configuration. $\boldsymbol{\tau} = J\boldsymbol{\sigma} = \det |\mathbf{F}| \boldsymbol{\sigma}$ is the Kirchhoff stress, with $\boldsymbol{\sigma}$ the Cauchy stress. \mathbf{f} is the traction on a surface with normal \mathbf{n} in the reference configuration, \mathbf{D} denotes the rate of deformation tensor, T is temperature, χ denotes the fraction of plastic work converted to heat, \mathbf{D}^p is the plastic part of \mathbf{D} , c_p is specific heat, k is thermal conductivity, (\cdot) denotes $\partial/\partial t$, $(\cdot)^{-1}$ and $(\cdot)^{-T}$ denote, respectively, inverse and inverse transpose. The dyadic product $\mathbf{A} : \mathbf{B}$ is $A^{ij} B_{ji}$. δT , $\delta \mathbf{D}$ and $\delta \dot{\mathbf{u}}$ denote admissible variations in temperature, rate of deformation and particle velocity, respectively. These two systems of equations are coupled through the heat generation term in Eq. (4).

Constitutive relation

Under the conditions of small elastic strains, assuming that the thermoelastic coupling is negligible and ignoring any temperature dependence of the elastic moduli [10], one can write the incremental stress-deformation rate relation as

$$\hat{\boldsymbol{\tau}} = \mathbf{L} : [\mathbf{D} - \mathbf{D}^p - \boldsymbol{\alpha} \dot{T}], \quad (5)$$

where $\hat{\boldsymbol{\tau}}$ is the Jaumann rate of Kirchhoff stress, \mathbf{L} is the tensor of elastic moduli, $\boldsymbol{\alpha}$ is the thermal expansion tensor and T is temperature. For isotropic, thermoelastic response,

$$\mathbf{L} = \frac{E}{1+\nu} \left[\mathbf{I}' + \frac{\nu}{1-2\nu} \mathbf{I} \otimes \mathbf{I} \right], \quad \boldsymbol{\alpha} = \alpha \mathbf{I}. \quad (6)$$

Here, \mathbf{I}' is the fourth order identity tensor, E is Young's modulus, ν is Poisson's ratio, α is the thermal expansion coefficient and $\mathbf{A} \otimes \mathbf{B}$ denotes the tensor product.

For an isotropically hardening viscoplastic solid, \mathbf{D}^p is given by

$$\mathbf{D}^p = \frac{3\dot{\bar{\epsilon}}}{2\bar{\sigma}} \boldsymbol{\tau}', \quad (7)$$

with $\dot{\bar{\epsilon}}$ being the equivalent plastic strain rate and

$$\boldsymbol{\tau}' = \boldsymbol{\tau} - \frac{1}{3}(\boldsymbol{\tau}:\mathbf{I})\mathbf{I}, \quad \bar{\sigma}^2 = \frac{3}{2}\boldsymbol{\tau}':\boldsymbol{\tau}'. \quad (8)$$

The thermoviscoplastic response of each of the constituent materials in the four microstructures is characterized by Eq. (1) and used in Eq. (7).

Boundary and initial conditions

The boundary and initial conditions applied for the microstructures shown in Fig. 2 are consistent with the conditions of the actual pressure–shear impact experiment. Details have been described in Ref. [3].

FINITE ELEMENT METHOD

Finite element discretization is based on triangular elements arranged in ‘crossed triangle’ quadrilaterals. Displacements and temperature are taken to vary linearly over the triangular elements. When the finite element approximations of the displacement and temperature fields are substituted into Eq. (3) [balance of momentum] and Eq. (4) [balance of energy], the resulting equations take the form,

$$\mathbf{M} \frac{\partial^2 \mathbf{U}}{\partial t^2} = \mathbf{R}, \quad (9)$$

and

$$\mathbf{C} \frac{\partial \mathbf{T}}{\partial t} = -\mathbf{K}\mathbf{T} + \mathbf{H}, \quad (10)$$

where \mathbf{U} is the vector of nodal displacements, \mathbf{T} is the vector of nodal temperatures, \mathbf{M} , \mathbf{C} and \mathbf{K} are, respectively, the mass, heat capacitance and heat conductance matrices, and \mathbf{R} and \mathbf{H} are the mechanical and thermal force vectors.

A lumped mass matrix is used in Eq. (9) for reasons of efficiency and accuracy [11]. Additionally, a lumped heat capacitance matrix is used in Eq. (10). In order to verify the accuracy of the integration of Eq. (10) with a lumped capacitance matrix, numerical results for a purely thermal problem involving non-uniform heat sources distributed on a rectangular area were compared with an analytical solution, and good agreement was found.

Equations (9) and (10) are decoupled and solved using a staggered scheme consisting of alternating isothermally mechanical and pure thermal processes. For each time step, the displacements and velocities are first obtained by integrating the equations of motion [Eq. (9)] using an explicit integration method, the Newmark β -method, with $\beta = 0$ and $\gamma = 0.5$, [12]. After the deformation field is obtained, $\boldsymbol{\tau}:\mathbf{D}^p$ is calculated and its contribution to the thermal force \mathbf{H} is determined. The temperature rates and temperatures are then obtained from Eq. (10). The rate tangent modulus expansion of Ref. [13] is used to update the stress tensor $\boldsymbol{\tau}$.

NUMERICAL RESULTS

First, the deformation of the base microstructure is considered. To illustrate the progression of shear deformation in the material, the distributions of equivalent plastic strain rate $\dot{\bar{\epsilon}}$ at 0.5, 1.0, 1.5 and 2.0 μs after impact are shown in Fig. 4. The impact velocity of this calculation is 200 ms^{-1} .

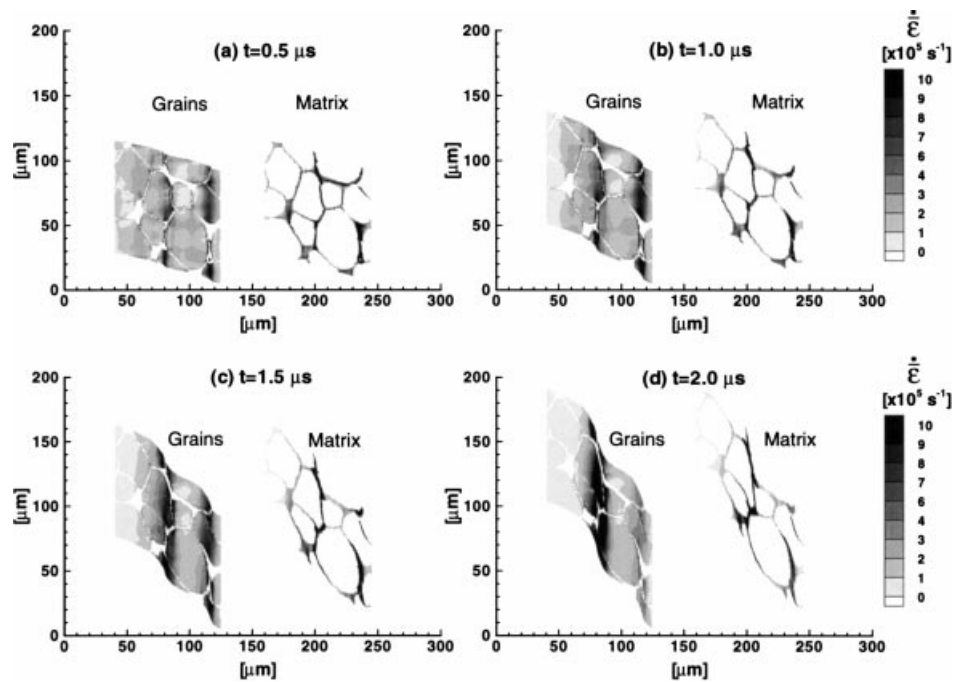


Fig. 4. Distributions of equivalent plastic strain rate at (a) 0.5 μs , (b) 1.0 μs , (c) 1.5 μs and (d) 2.0 μs after impact for the base microstructure at an impact velocity of 200 ms^{-1} .

For clear presentation of the data, the grains and the matrix are plotted separately. This is the format that will be used throughout this paper. Later when the microstructure with an additional interfacial layer [Fig. 2(b)] is considered, the interfacial layer is plotted together with the matrix, while the grains are plotted separately. The progression of shear deformation is clear in Fig. 4 as the microstructure deforms. Initially, there are two bands of high rates of deformation: one of the two bands is located near the right side of the material block (the impact face in the pressure–shear configuration of Fig. 1) and the other is located in the middle of the material block. The rates of deformation in the middle band increase with time. Eventually, this band becomes fully developed and the rate of deformation in the band closer to the impact face decreases. As a result, deformation localizes into only one of the two competing bands. Note that the equivalent plastic strain rate is high in both the grains and the matrix for the part of the material that is involved in the shear bands.

Figure 5 shows profiles of equivalent plastic strain rate $\dot{\bar{\epsilon}}$ [Fig. 5(a)], equivalent plastic strain $\bar{\epsilon}$ [Fig. 5(b)], temperature [Fig. 5(c)] and shear stress component σ_{12} of the Cauchy stress $\boldsymbol{\sigma}$ [Fig. 5(d)] across the specimen thickness. The results are from the same calculation as that of Fig. 4. The curves reflect average values of the quantities in the ξ^2 direction. The profiles show variations across the specimen thickness (in the ξ^1 direction) at 0.4, 0.8, 1.2, 1.6 and 2.0 μs after the beginning of the deformation. The growth of the two competing shear bands is clear. Initially, both bands have similar rates of deformation, levels of plastic strain and values of temperature. After approximately 1.5 μs following the beginning of the deformation, more deformation occurs in the central band and deformation gradually localizes into the middle region of the specimen. The conduction of heat through the impact face contributed to reducing the deformation in the band that is closer to the impact face. The error bars in Fig. 5(c) show the range of temperature

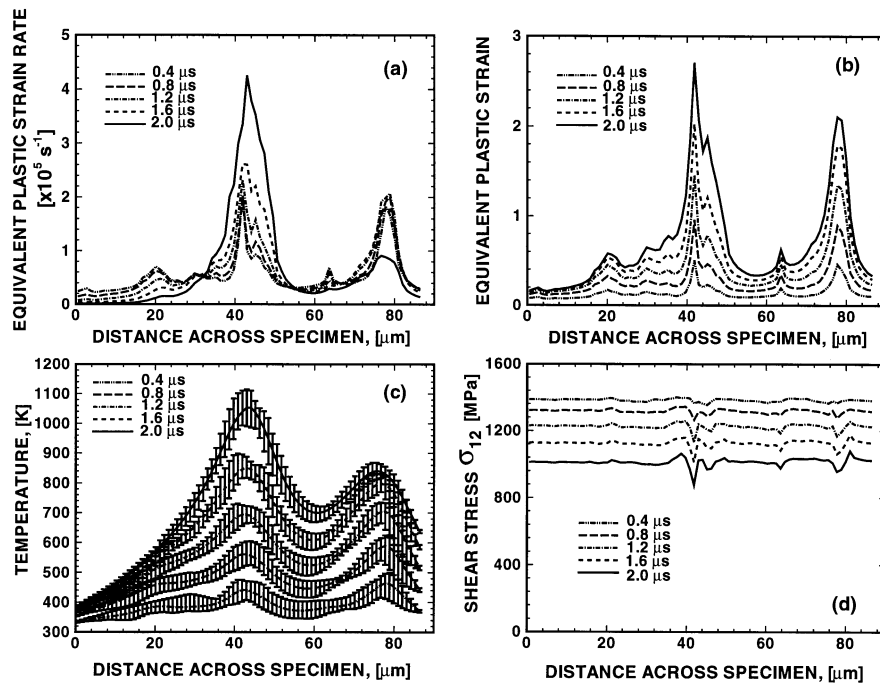


Fig. 5. Distribution of (a) $\dot{\bar{\epsilon}}$, (b) $\bar{\epsilon}$, (c) temperature, and (d) σ_{12} at $2 \mu\text{s}$ after impact for the base microstructure at an impact velocity of 200 ms^{-1} .

differences along the shear bands (shear direction) for fixed ξ^1 values. Figure 5(d) shows that as the deformation progresses, thermal softening causes the overall shear stress carried by the composite to decrease. Across the specimen thickness, shear stress σ_{12} is rather uniform, except for locations near the centres of the shear bands after they are well developed. This uniformity makes it reasonable to use, e.g. the average shear stress at the impact face along the ξ^2 direction to represent the stress level carried by the overall composite as the deformation progresses. The evolution of the curves clearly shows the development of the shear bands. The curves will be used later to compare the effects of the microstructural variations on the localization process.

Figure 6 compares the distributions of $\dot{\bar{\epsilon}}$ at $2 \mu\text{s}$ after impact for the four microstructures in Table 1. The impact conditions are the same for all the microstructures with an impact velocity of 200 ms^{-1} and an impact angle of 26.6° . The four contour plots (a–d) correspond to the four microstructures in Table 1 in the same order. Figure 6(a) corresponds to the base microstructure. Figure 6(b) corresponds to microstructure (b) with a matrix having a lower thermal conductivity. Figure 6(c) corresponds to microstructure (c) which has an interfacial layer of low conductivity. Figure 6(d) corresponds to microstructure (d) which has a matrix with a higher rate of thermal softening. The corresponding distributions of $\dot{\bar{\epsilon}}$ across the specimen thickness for the four cases at five different times after impact are shown in Fig. 7. The curves represent average values in the ξ^2 direction, similar to those in Fig. 5.

Compared with those in Figs 6(a) and 7(a), the results in Figs 6(b) and 7(b) show that decreasing the thermal conductivity of the matrix from $k_m = 100 \text{ W(m} \cdot \text{K)}^{-1}$ to $25 \text{ W(m} \cdot \text{K)}^{-1}$ allow both bands in the specimen to become fully developed. At $2 \mu\text{s}$, these two bands have equal rates of deformation. As a result, each band has lower rates of deformation than those in the central band

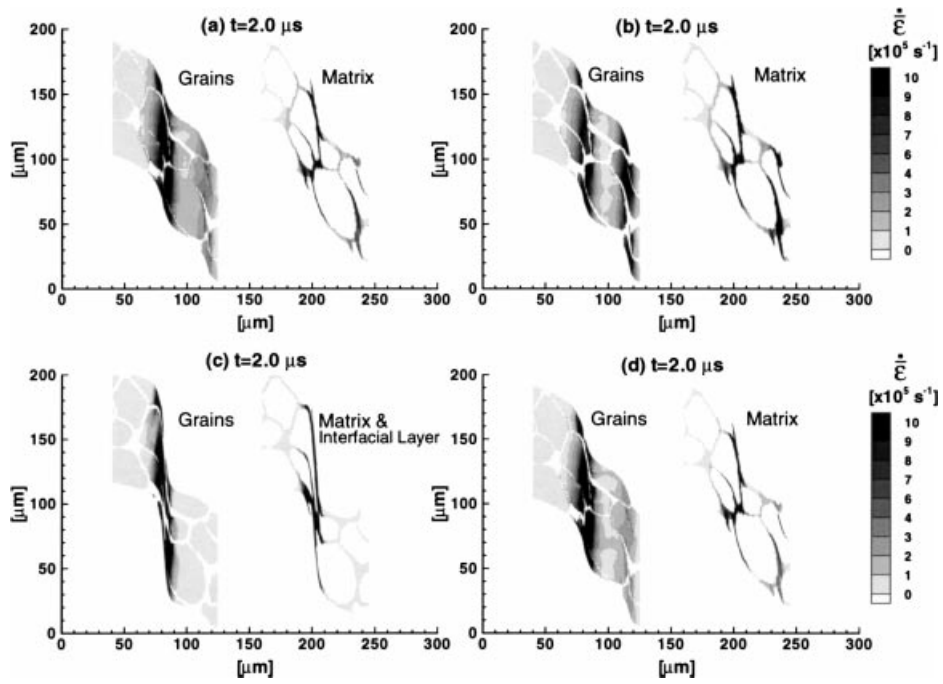


Fig. 6. A comparison of the distributions of $\dot{\epsilon}$ at 2 μs after impact for (a) the base microstructure, (b) microstructure, (c) microstructure, and (d) microstructure at an impact velocity of 200 ms^{-1} .

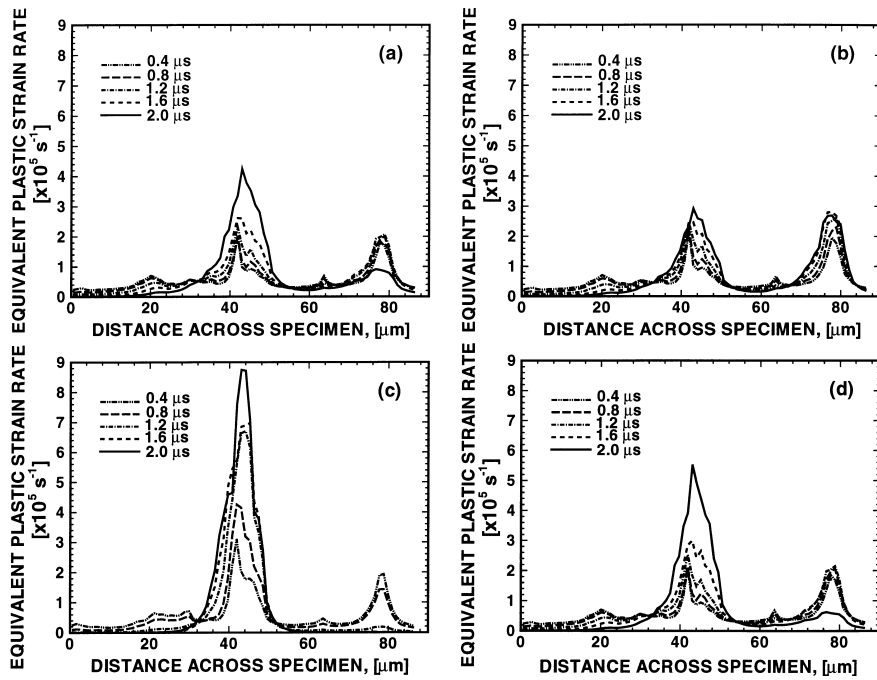


Fig. 7. A comparison of the evolutions of $\dot{\epsilon}$ for microstructures (a–d) at an impact velocity of 200 ms^{-1} .

that is fully developed in Figs 6(a) and 7(a). It will be shown later that this leads to less thermal softening in each band and higher overall stress levels in the composite at the same nominal shear strains, compared with the results in Figs 6(a) and 7(a).

Figures 6(c) and 7(c) show that the addition of an interfacial layer with a lower thermal conductivity significantly expedites the development of shear bands. This is because the lower thermal conductivity retards heat exchange between the grains and the matrix. Note that the matrix is softer, therefore, deforms more and generates more heat. The reduced heat exchange causes the temperature increase in the matrix to be higher compared with that in the case without the interfacial layer. This difference begins to accumulate as soon as plastic deformation starts. Consequently, the composite exhibits lower levels of flow stress compared with microstructure (a). Also, the total amount of shear strain accumulated is higher compared with the two microstructures considered so far. Furthermore, the rates of deformation are significantly higher compared with the base microstructure [Figs 6(a) and 7(a)] and microstructure (b) [Figs 6(b) and 7(b)].

The alteration of the matrix to one with a higher rate of thermal softening at temperatures above 1000 K does not significantly change the deformation for the time period shown in Figs 6 and 7 (up to $2 \mu\text{s}$ after the beginning of deformation). It is clear that the results in Figs 6(a) and 6(d) are very similar to each other. The similarity can also be seen in Figs 7(a) and 7(d). The lack of difference in the results indicates that for the duration of deformation discussed, the higher rate of thermal softening at high temperatures in microstructure (d) has not been fully activated. However, calculations beyond $2 \mu\text{s}$ show that once the temperature reaches levels above T_c [which is chosen to be 1300 K and 1000 K in Figs 6(a) and 6(d), respectively], the accelerated thermal softening does have a clear influence on the deformation. This effect can be seen in the stress–strain curves in Fig. 8. The four curves shown are the nominal shear stress–strain relations for the four cases considered in Figs 6 and 7. The nominal shear strain in this figure is obtained by dividing the relative displacements at the left and right faces of the specimen by its original thickness. Shear stress σ_{12} is the average value of the shear component of the Cauchy stress tensor at the impact (right) face. It can be seen from Fig. 8 that the stress–strain curves for microstructures (a) and (d) are close for shear strains up to 1.1, after which the curve for Fig. 6(d) drops more rapidly, signifying a more rapid loss of stress-carrying capacity due to the higher rate of thermal softening at high temperatures. Clearly, microstructural variation (d) represents a change that allows the composite to retain a relatively high level of flow stress for deformation up to a certain strain level ($\gamma = 1.1$) while permitting more rapid loss of strength beyond this critical amount of strain.

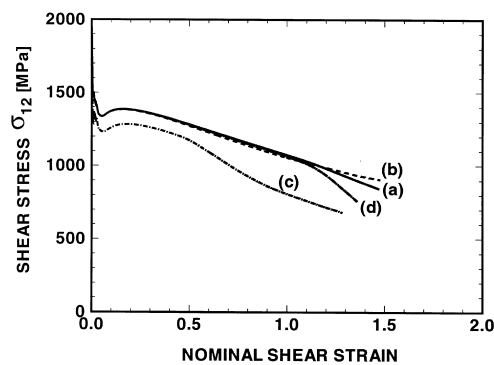


Fig. 8. A comparison of the shear stress–strain curves for microstructures (a–d) at an impact velocity of 200 ms^{-1} .

Microstructural variation (b) which represents a composite with a lower thermal conductivity for the matrix gives rise to a stress–strain curve that closely follows that of the base microstructure for shear strains up to 1.2. At larger strains, this microstructure carries stresses higher than those for the base microstructure. This is due to the fact that two shear bands exist in (b). Consequently, the amount of deformation and temperature increase in each band is lower, limiting the amount of thermal softening available for further loss of strength. This result shows that strain localization in inhomogeneous microstructures and the evolution of stress-carrying capacities of composite materials are not only influenced by factors such as thermal softening and heat conduction, but they are also significantly influenced by the material inhomogeneities inherent in the microstructures. The use of a larger representative microstructural area may help to demonstrate the effect of the lower level of thermal conductivity in microstructure (b).

Microstructural variation (c) shows a stress–strain curve that is significantly lower than that of the base microstructure and those of variations (b) and (d). Clearly, the very low thermal conductivity of the interfacial layer plays a significant role in retarding the flow of heat between the matrix which is softer (therefore, deforms more and generates more heat than the grains) and the grains which are harder. This retardation results in higher temperatures and stronger softening throughout the deformation compared with the base microstructure, thus causing the deformation to progress at lower overall stress levels.

DISCUSSION AND SUMMARY

Numerical calculations are carried out to analyse the effects of three potentially useful variations in the microstructure of a class of tungsten composites. The results have identified three microstructural configurations that expedite the localization of dynamic shear deformation. Furthermore, the results showed that it is possible to retain the high levels of flow stress for initial deformation up to a certain degree while achieving enhanced localization. The calculations have indicated that the inhibition of heat exchange between the phases can play a significant role in promoting the formation of shear bands and the loss of stress-carrying capacity of the composite materials. While the addition of an interfacial layer of low conductivity does enhance localization, there is also a consistent reduction in the flow stress level of the composite material throughout the deformation. It is not clear whether this reduction in stress would improve the performance of penetrators by providing better opportunities for failure through the expedition of shear band formation or adversely affect the performance by lowering the dynamic strength of the materials. Further analysis is needed to determine the overall influence of this microstructure on the performance of penetrators. The modification of the matrix phase to one having a higher rate of thermal softening at high temperatures allows the composite materials to retain high levels of flow stress while expediting the localization of strain and loss of strength at strains beyond a certain level. This variation seems to be a desirable microstructural configuration that may provide the combination of material properties needed for better penetration performance. The effect of lowering the thermal conductivity of the matrix should be further analysed using a larger representative microstructural area.

The analysis carried out here has focused on the effects of three individual variations from one base microstructure. This is partly motivated by the need to delineate and characterize the influence of different factors separately. Clearly, combinations of these variations and other microstructural modifications can be used. Such combinations may well provide more effective means to enhance localization while allowing the materials to retain high flow stresses. For example, variations (c) and (d) can be used simultaneously. In addition, since these variations expedite shear band formation, one may consider increasing the volume fraction of the stronger phase, the grains, to

increase the flow stress. The increase in flow stress derived from the larger fraction of grains can offset the decrease caused by the addition of the interfacial layer, therefore providing for enhanced propensity for localization while retaining or increasing the level of flow stresses at small strains.

While the numerical calculations may have pointed out certain favourable changes, the implementation of these changes in actual material engineering poses its own challenges. First, material systems and compositions that can produce such desired changes must be identified. The nickel–cobalt matrix composite analysed by Lankford *et al.* [14] demonstrated a combination of strong initial strain hardening and high levels of flow stress that are desirable characteristics of an improved material. It may be useful to identify a practical approach to modify this Ni–Co matrix so it attains a higher rate of thermal softening at high temperatures as well. This will give a combination of high initial strength and the ability to lose strength at large strains to this existing material.

Recently, efforts have been made to use hafnium as the matrix phase in tungsten composites to replace the traditional nickel–iron–tungsten matrix [15]. While the relatively weak rate sensitivity is favourable to enhancing the localization of the strains, the strong strain hardening exhibited by hafnium throughout the deformation and its relatively high melting point (2500 K) seem to work against a stronger driving force for localization, considering that the melting temperature of the traditional Ni–Fe–W matrix is approximately 1750 K. Indeed, the lack of shear localization in the tungsten–hafnium specimens in the impact experiments of Yadav and Ramesh [15] may be an indication of the relatively weak propensity for shear localization in this type of microstructures. Microstructural changes are needed in order for this type of matrix to be used for better localization behaviour.

In addition to changes in the thermomechanical behaviour of the constituents, microstructural variations also include morphological changes, e.g. phase distribution, phase volume fraction and phase size. These variations can be derived from alterations in chemical composition, material processing and heat treatment. This paper has focused on changes in the thermomechanical properties of the individual phases only. Zhou *et al.* [3] studied the effects of certain morphological variations, e.g. phase volume fraction, grain shape, grain arrangement and grain size. So far, these analyses have not considered failure mechanisms, e.g. grain fracture, matrix rupture and phase boundary sliding, which have been shown to be responsible for the eventual failure of the materials inside intensely formed shear bands under the conditions considered [4]. Nevertheless, the results obtained are useful in characterizing the effects of microstructure on the dynamic behaviour of a whole class of composite materials. The calculations carried out here represent one step of a systematic mechanics and materials approach in improving the performance of a class of composite materials in an application which demands a combination of high strength and failure through localized deformation at large strains.

Acknowledgement—Analysis in later stages of this work was supported by the Office of Naval Research through grant number N00014-96-1-1195. The calculations were carried out on Cray supercomputers at the Jet Propulsion Laboratory and the Goddard Space Center.

REFERENCES

1. L. S. Magness (1994) High strain rate behaviors of kinetic energy penetrator materials during ballistic impact. *Mech. Mat.* **17**, 147–154.
2. M. Zhou, R. J. Clifton and A. Needleman (1992) Shear band formation in a W–Ni–Fe alloy under plate impact. *Proc. Int. Conf. on Tungsten and Tungsten Alloys*, November, Arlington, VA, pp. 343–356.
3. M. Zhou, A. Needleman and R. J. Clifton (1994) Finite element simulations of dynamic shear localization. *J. Mech. Phys. Solids* **42**, 423–458.

4. M. Zhou and R. J. Clifton (1997) Dynamic constitutive and failure behavior of a two-phase tungsten composite. *J. Appl. Mech.* **64**, 487–494.
5. E. W. Andrews, A. F. Bower and J. Duffy (1992) Shear band formation in a tungsten heavy alloy. In: *Proc. Symposium on Shear Bands and Viscoplastic Theories, The 29th Annual Technical Meeting of the Soc. for Engng Sci.*, 14–16 September, La Jolla, CA.
6. T. Weerasooriya, P. A. Beaulieu and R. Swanson (1992) Deformation and failure behavior of 93W–5Ni–2Fe at high strain rate shear loading. U.S. Army Materials Technology Laboratory Report, No. MTL TR 92-19, Watertown, MA.
7. J. LeMonds and A. Needleman (1986) Finite element analyses of shear localization in rate and temperature dependent solids. *Mech. Mater.* **5**, 339–361.
8. A. Needleman (1989) Dynamic shear band development in plane strain. *J. Appl. Mech.* **56**, 1–9.
9. A. Needleman and V. Tvergaard (1991) An analysis of dynamic, ductile crack growth in a double edge cracked specimen. *Int. J. Fract.* **49**, 41–67.
10. G. L. Povirk, S. R. Nutt and A. Needleman (1993) Continuum modelling of residual stress in metal-matrix composites. *TMS Annual Meeting Proceedings, Residual Stresses in Composites: Measurement, Modelling and Effect on Thermo-mechanical Properties*.
11. R. D. Krieg and S. W. Key (1973) Transient shell response by numerical time integration. *Int. J. Numer. Meth. Engng* **7**, 273–286.
12. T. Belytschko, R. L. Chiapetta and H. D. Bartel (1976) Efficient large scale non-linear transient analysis by finite elements. *Int. J. Numer. Meth. Engng* **10**, 579–596.
13. D. Pierce, C. F. Shih and A. Needleman (1984) A tangent modulus method for rate dependent solids. *Comp. Struct.* **18**, 875–887.
14. J. Lankford, A. Bose, H. Couque and C. E. Anderson (1991) *Proc. 12th Army Symposium on Solid Mechanics*, Plymouth, MA, pp. 117–138.
15. S. Yadav and K. T. Ramesh (1995) The mechanical properties of tungsten-based composites at very high strain rates. *Mater. Sci. Engng A* **203**, 140–153.